

Article

LA-ICP-MS Trace-Element Analysis of Pyrite from the Huanxiangwa Gold Deposit, Xiong'ershan District, China: Implications for Ore Genesis

Fuping Gao ^{1,*} , Yangsong Du ^{1,*}, Zhenshan Pang ², Yilun Du ², Fengpei Xin ³ and Jinsong Xie ³¹ School of the Earth Sciences and Resources, China University of Geosciences, Beijing 100083, China² Development and Research Center of China Geological Survey, Beijing 100037, China; pangzs835@163.com (Z.P.); dylbeijing@163.com (Y.D.)³ No. 1 Institute of Geological and Mineral Resources Survey of Henan, Luoyang 471023, China; cugbxfp@hotmail.com (F.X.); shanchengxiaozyhu@163.com (J.X.)

* Correspondence: gfp2000@163.com (F.G.); duys5510@cugb.edu.cn (Y.D.)

Received: 24 January 2019; Accepted: 1 March 2019; Published: 6 March 2019



Abstract: The Huanxiangwa deposit is a major gold deposit in the Xiong'ershan district, which is the third-largest gold-producing district in China. Pyrites from the Huanxiangwa deposit were investigated using ore microscopy and laser ablation-inductively coupled plasma-mass spectrometry (LA-ICP-MS). Pyrite is the dominant Au-bearing mineral in the Huanxiangwa deposit and can be divided into two types: medium- to fine-grained subhedral-anhedral pyrite (Py1) disseminated in altered rocks and coarse-grained subhedral-euhedral pyrite (Py2) hosted in auriferous quartz veins. LA-ICP-MS time-resolved depth profiles show that invisible gold occurs primarily as solid solution or as homogeneously distributed nanoparticles of native gold, electrum, or Au-Ag-Te minerals in Py1, whereas it is present mainly as nano- to submicron-sized inclusions of complex Au-Ag-Cu-Pb-Zn domains in Py2. The presented data indicate that the Huanxiangwa deposit resulted from two episodes of hydrothermal mineralization associated with two distinct source reservoirs. The first episode of mineralization was linked to the dehydration of deep-seated mafic-ultramafic metamorphic rock during the Triassic collision of the North China Craton with the Yangtze Craton. The second episode of mineralization was related to hydrothermal activity resulting from Early Cretaceous I-type granitic magmatism.

Keywords: LA-ICP-MS; trace elements; pyrite; gold mineralization; Xiong'ershan

1. Introduction

The North China Craton (NCC) contains several large gold deposits and supplies almost 70% of China's gold production [1,2]. The Xiong'ershan gold field is situated in the southern margin of the NCC (Figure 1a) and is the third-largest gold-producing district in China [3,4]. Most of the gold deposits in the Xiong'ershan area are located to the north of the Machaoying Fault and are hosted in Neoproterozoic metamorphic rocks and late Paleoproterozoic volcanic rocks (Figure 1b). These deposits have been extensively studied during the last two decades [3,5–7], but their genesis remains controversial. Several different interpretations have been proposed, including (i) the gold deposits are of greenstone type [8], associated with the occurrence of Neoproterozoic high-grade metamorphic rocks that provided the source material for the metallogenesis [2]; (ii) the deposits are orogenic gold deposits that formed during a Mesozoic continental collision regime, with the gold-mineralizing fluids originating mainly from metamorphic dehydration and mixing with meteoric water [3,5,9]; and (iii) the deposits have a late Mesozoic magmatic-hydrothermal origin [6,7,10,11].

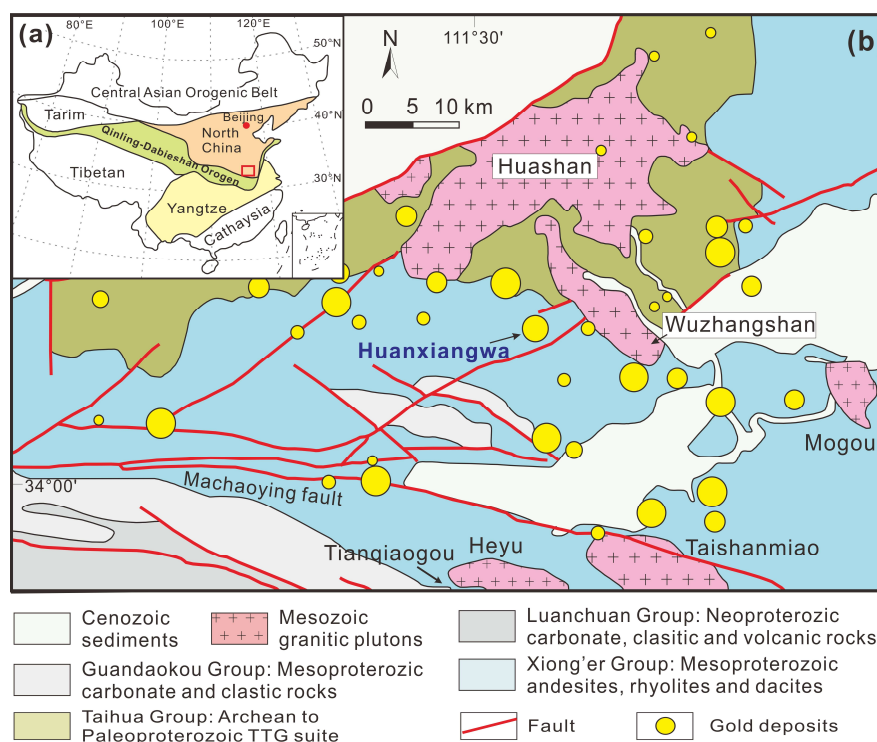


Figure 1. (a) Simplified structural map of China showing the major tectonic subdivisions and the location of the Xiong'ershan gold district [12,13]. (b) Simplified geological map showing the distribution of gold deposits in the Xiong'ershan area [12].

Pyrite is the most important Au-bearing mineral in the Xiong'ershan district [3,5]. Previous investigations have shown that pyrite is stable under a wide range of physicochemical conditions and, in contrast to other sulfides, exhibits refractory behavior with respect to post-depositional metamorphic processes [14–16]. These features make pyrite a suitable mineral for reconstructing the processes of ore formation [15,17]. In addition, previous studies have shown that the incorporation of gold into pyrite is controlled mainly by As in the case of As-rich pyrite and by Te in the case of As-free pyrite [17–21]. The structure of pyrite becomes distorted when As or Te are incorporated, favoring the entry of relatively large Au^+ ions into the structure [22,23]. Some of the pyrites in the Xiong'ershan district are known to have an As-free and low-Te signature [3]. The characteristics of the deposits in this ore district are therefore favorable for investigating the distribution of invisible gold in pyrite.

The Huanxiangwa deposit is a large and representative gold deposit of the Xiong'ershan ore district. In this paper, we report the results of a laser ablation-inductively coupled plasma-mass spectrometry (LA-ICP-MS) analysis of pyrite in the Huanxiangwa deposit, based on which we infer the mineralization processes that led to the formation of the deposit and present a new model of ore genesis.

2. Geological Setting

The Xiong'ershan ore district is located in the southern margin of the NCC (Figure 1a) and is bounded by the Machaoying Fault to the south and the Luoning Fault to the northwest (Figure 1b). The Xiong'ershan ore district contains more than 20 gold deposits, with most being hosted in Taihua Group metamorphic rocks and Xiong'er Group volcanic rocks. The Taihua Group comprises a high-grade metamorphic sequence of amphibolite- to granulite-facies rocks [24,25]. This group consists mainly of plagioclase-amphibole gneiss, biotite-plagioclase gneiss, amphibolite, granulite, and quartz schists, all of which belong to a tonalite–trondhjemite–granodiorite (TTG) suite [26]. The whole-rock Sm-Nd and zircon U-Pb ages of the amphibolite- to granulite-facies rocks of the Taihua Group are 2.84–2.26 Ga [26–28]. The Xiong'er Group comprises a succession of low-grade volcanic rocks (3.0–7.6 km thick) that

together cover an area of >6000 km² [29]. The volcanic rocks are divided into the Xushan, Jidanping, and Majiahe formations [29]. These volcanic rocks consist mostly of andesite and basaltic andesite together with subordinate dacite and rhyolite [29] and yield zircon U-Pb ages of 1.80–1.75 Ma [29,30].

Mesozoic igneous rocks are widespread in the Xiong'ershan area and occur as large batholiths (e.g., Wuzhangshan, Huashan, and Heyu) or small porphyritic bodies (e.g., Lemengou, Qiyugou, and Banzhusi) (Figure 1b). These plutons comprise mostly biotite granite, biotite amphibole granite, monzogranite, and syenogranite, and they intrude the Archean to Paleoproterozoic rocks of the Taihua and Xiong'er groups. High-precision zircon U-Pb dating of the intrusive rocks in the Xiong'ershan district using LA-ICP-MS and sensitive high resolution ion micro probe (SHRIMP) methods yields Late Jurassic–Early Cretaceous ages (mainly 163–113 Ma) [31–34].

The E–W trending Machaoying Fault and the NE–SW trending Luoning Fault are the major structures in the Xiong'ershan district. The Machaoying Fault is >200 km long and 5 km wide, reaches depths of 34–38 km, and dips 50°–80° to the NNE [35]. This fault is considered to have been an important control on the formation and distribution of gold deposits in the Xiong'ershan district. The Machaoying Fault has been interpreted from geophysical data as a major fracture cutting the crust and extending into the lithospheric mantle [36]. The Luoning Fault is located in the northwestern Xiong'ershan district and juxtaposes late Mesozoic sedimentary sequences against Archean metamorphic rocks [6]. Several NE–SW trending secondary or minor faults are developed in the area north of the Machaoying Fault (Figure 1b).

3. Deposit Geology

The Huanxiangwa gold deposit is located in the central part of the Xiong'ershan ore district (Figure 1b). The stratigraphic sequence exposed in the deposit comprises the Xushan and Jidanping formations of the Xiong'er Group (Figure 2). The Xushan Formation consists predominantly of andesite and basaltic andesite with minor mugearite and tuff. The Jidanping Formation is dominated by rhyolite and dacite interlayered with andesite and basaltic andesite. The orebodies are typically found in alteration zones developed along the NW–SE trending Huanxiangwa F985 Fault. This fault is ~3000 m long and 10–30 m wide and dips ~29° to the NE. The only exposed Mesozoic intrusion near the mining area is the Wuzhangshan monzogranite (Figure 2), which intrudes Xiong'er Group volcanic rocks in the Huanxiangwa gold deposit. The rocks of this intrusion are generally reddish to pinkish porphyritic monzogranites consisting of 3%–6% phenocrysts (mainly plagioclase, with lesser K-feldspar) in a medium-grained granular matrix of K-feldspar, plagioclase, quartz, amphibole, and minor biotite. The main accessory minerals are zircon, titanite, magnetite, and apatite. The Wuzhangshan monzogranites show relatively high Sr contents, high Sr/Y and (La/Yb)_N ratios, and low Y and Yb contents, indicating an adakitic affinity [37]. Detailed geochemical and Sr-Nd-Pb isotopic data show that the Wuzhangshan monzogranites originated from the partial melting of Neoproterozoic–Paleoproterozoic Taihua Group metamorphic basement rocks [37]. Zircon U-Pb ages for the Wuzhangshan monzogranites range between 153.6 ± 1.3 and 163.3 ± 2.1 Ma [4,31,33].

The Huanxiangwa gold deposit is located ~50 km northwest of Songxian County, Henan Province, and was discovered in the early 1980s. The deposit has a gold resource of ~30 t with an ore grade of ~4.7 g/t. Gold mineralization is hosted within the Xushan andesite of the Xiong'er Group. The deposit contains 10 orebodies, with the largest, the No. 1 orebody, showing mineralization features that are representative of the deposit. The No. 1 orebody is structurally controlled by the F985 Fault (Figure 2a,b) and contains >80% of the known reserves of the Huanxiangwa deposit [38]. This orebody strikes 90°–110°, dips 20°–40° to the NE, is ~1300 m long and 0.6–22.2 m thick, and is continuous between the 1230 and 620 m ore-mining elevations.

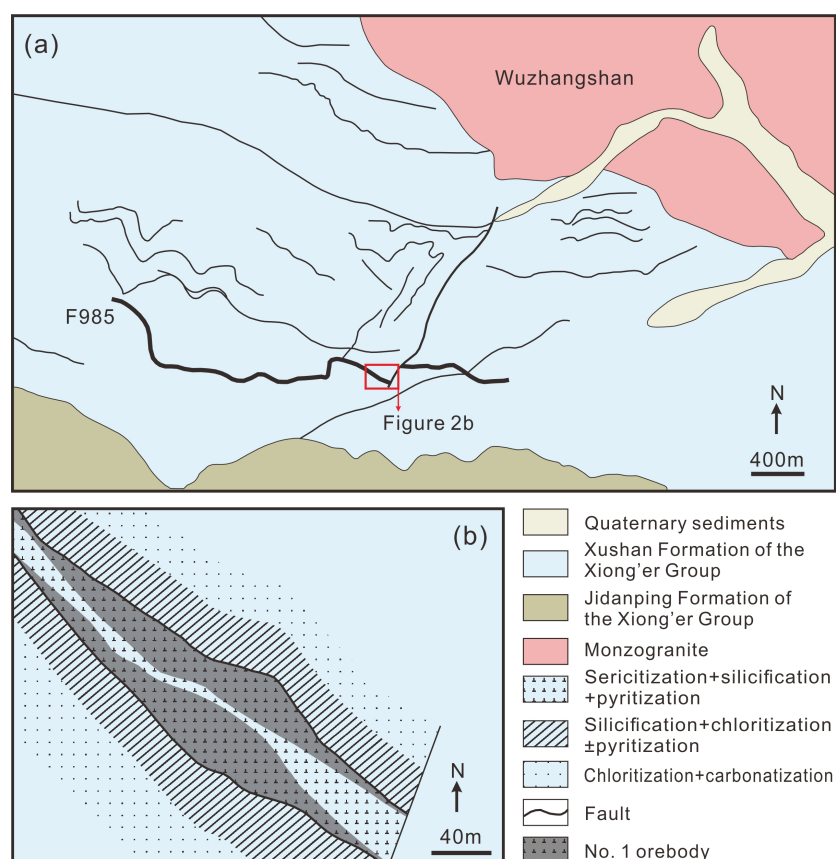


Figure 2. Simplified geological maps of (a) the Huanxiangwa district and (b) the No. 1 orebody of the Huanxiangwa deposit [38].

4. Pyrite Types and Textures

Two mineralization styles are found in the Huanxiangwa deposit: disseminated in altered rocks (type 1) and auriferous quartz veins (type 2). The type 1 ore is economically the most important mineralization type of the deposit. Hydrothermal alteration associated with type 1 ore is well developed and includes silicification, sericitization, chloritization, carbonatization, and pyritization. The alteration zone ranges from 20 to 100 m in width and contains variable quantities of metallic minerals including disseminated pyrite. The occurrence of gold is closely associated with the distribution of sericitization and pyritization (Figure 2b). The boundaries between the wall-rocks and the orebodies are transitional rather than sharp and can be defined only by the ore cut-off grade. The textures of type 1 ore are primarily relicts of metasomatism and are anhedral granular (Figure 3a,b). The ore minerals are disseminated and are dominated by pyrite together with minor arsenopyrite and galena (Figure 3a,b), whereas the gangue minerals include feldspar, quartz, calcite, sericite, and chlorite. Type 2 ore occurs as veins and cross-cuts the type 1 ore (Figure 3c), with the auriferous quartz veins generally having a thickness of 0.1–2.0 m. The ore textures are mainly euhedral granular (Figure 3d–f). The minerals of type 2 ore include pyrite, chalcopyrite, sphalerite, and galena, and the gangue minerals are quartz, calcite, and fluorite (Figure 3d–f). In both types of ore, visible gold occurs predominantly as native gold and electrum and commonly forms grains within pyrite as well as along boundaries within or between mineral microfractures (Figure 3g,h). Electron microprobe analyses show that native gold consists of 92.1 wt %–92.2 wt % Au and 7.1 wt %–7.3 wt % Ag, corresponding to a gold fineness of 926–928, whereas the electrum has ~81.6 wt % Au and ~17.1 wt % Ag, with a gold fineness of ~827 [39].

Pyrite is the most common Au-bearing sulfide mineral in the Huanxiangwa deposit and can be divided into two types based on its morphology and the host rock type: (1) Py1 is distributed in type 1 ores (disseminated in altered rocks) and comprises medium- to fine-grained subhedral-anhedral pyrite

with sizes of 20–300 μm (Figure 3a,b) and (2) Py2 is found in type 2 ores (auriferous quartz veins) and occurs as aggregates dispersed in quartz veins, consisting of coarse-grained, subhedral-euhedral crystals with a cubic or pyritohedral form that typically exceed 500 μm in diameter (Figure 3d–f). Chalcopyrite, sphalerite, and galena inclusions are observed locally in Py2 (Figure 3i).

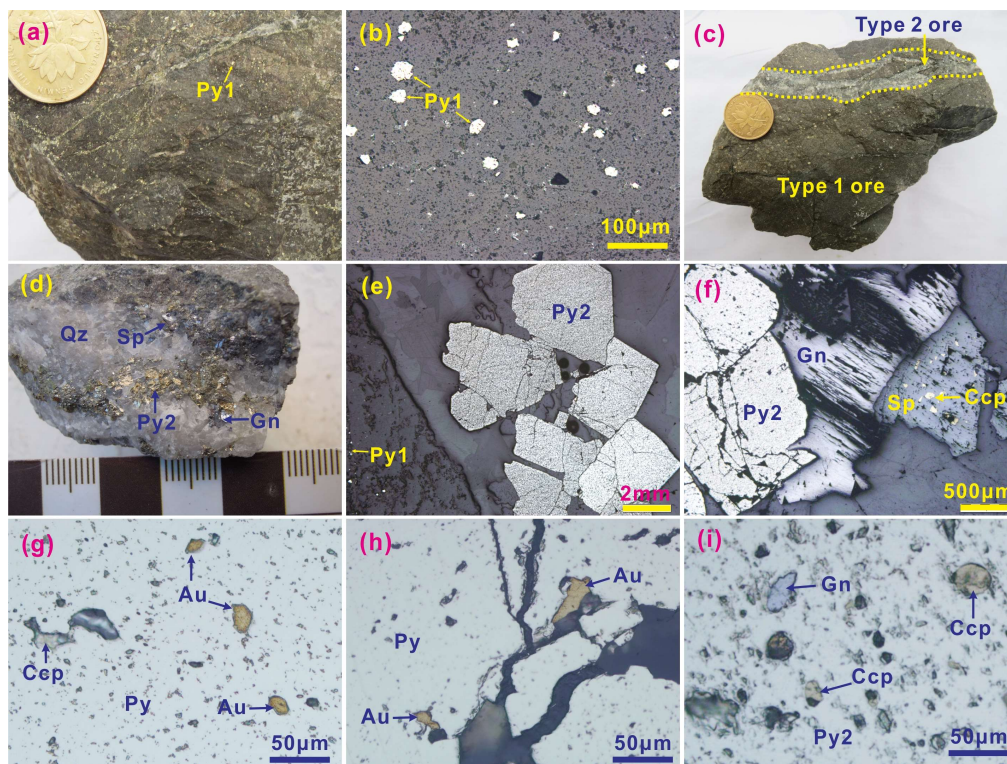


Figure 3. Hand-specimen photographs and reflected-light ore petrography of the Huanxiangwa gold deposit. (a,b) Fine-grained anhedral pyrite (Py1) disseminated in altered rocks; (c) auriferous quartz vein (type 2 ore) cross-cutting disseminated ore (type 1 ore); (d–f) coarse-grained, subhedral-euhedral pyrite (Py2) in an auriferous quartz vein; (g,h) native gold and electrum in fractures or as inclusions in pyrite; (i) chalcopyrite and galena inclusions in Py2. Type 1 ore—disseminated ore; Type 2 ore—auriferous quartz vein; Py—pyrite; Py1—pyrite disseminated in altered rocks; Py2—pyrite hosted in auriferous quartz veins; Ccp—chalcopyrite; Gn—galena; Sp—sphalerite; Au—visible gold; Qz—quartz.

5. Samples and Analytical Technique

Twenty samples were collected from the two types of ore and polished into thin-sections for petrographic observations. Of these 20 samples, 8 were selected for pyrite trace-element analysis. As gold and sulfide inclusions were present in the pyrite, all pyrites were first inspected using reflected-light microscopy to avoid native gold grains or other discrete sulfide minerals within the pyrite during analysis.

Trace-element concentrations in pyrite were determined using LA-ICP-MS on polished thin-sections at the Research School of Earth Sciences, Australian National University, Canberra, Australia, with a single-collector quadrupole Agilent 7700 ICP-MS instrument (Hachioji, Japan). The analyses were performed by ablating spots with diameters of 30–62 μm (depending on pyrite size) using a repetition rate of 5 Hz and an output energy of ~30 mJ. The analysis time for each sample was 80 s, which included 40 s of background measurement with the laser off and 40 s of analysis with the laser on. The acquisition time for all materials was set to 0.01–0.03 s, with a total sweep time of ~0.5 s. Data reduction was performed using Iolite [40], with Fe being adopted as the internal standard. The analyses of pyrite were calibrated using the standards STDGL3 and CANMET Po727. Au and Pt were calibrated to CANMET Po727, and the remaining elements were calibrated to STDGL3.

Trace-element concentrations in each sampled mineral, as well as the detection limits, were calculated following the methods of Longerich et al. [41].

6. Results

A total of 39 LA-ICP-MS spot analyses were conducted on pyrites from selected samples, including 18 spots on Py1 and 21 spots on Py2. Element contents and their variations in the two types of pyrite are presented in Table 1 and Figure 4.

Table 1. LA-ICP-MS results for pyrites from the Huanxiangwa gold deposit.

Sample No.	Au	Ag	Cu	Pb	Zn	Co	Ni	As	Te
Py1									
APY-1	2.65	34.9	48.8	37.5	1.46	459	559	730	39.2
APY-2	0.80	15.2	26.4	23.8	1.86	181	303	171	21.8
APY-3	1.38	19.6	33.4	18.4	1.22	347	493	289	29.0
APY-4	0.33	5.70	21.1	23.0	4.40	229	264	52.4	9.60
APY-5	3.78	83.0	41.4	32.5	7.90	380	321	342	62.4
APY-6	0.90	4.38	37.9	259	3.84	554	533	280	6.60
APY-7	0.73	3.09	38.0	77.2	1.36	415	394	164	4.18
APY-8	1.84	31.9	41.1	1880	2.48	429	459	422	14.2
APY-9	1.41	7.40	72.0	92.8	2.43	452	271	46	10.2
APY-10	0.80	3.72	60.0	730	8.50	710	441	448	6.56
APY-11	0.44	8.00	30.3	102	17.4	453	364	121	3.41
APY-12	2.07	12.5	62.0	750	3.54	453	438	38.5	14.5
APY-13	4.30	5.50	23.2	68.4	2.96	319	426	178	8.00
APY-14	1.08	3.04	45.0	94.7	2.02	337	370	270	6.64
APY-15	0.77	14.9	52.2	700	5.70	350	365	185	7.50
APY-16	2.60	47.7	74.0	12,600	19.6	806	627	1060	10.0
APY-17	1.09	4.43	132	102	2.80	830	163	18.4	6.59
APY-18	1.16	200	84.0	179	7.50	815	171	30.6	19.5
Average	1.56	28.1	51.3	987	5.39	473	386.8	269	15.5
RSD	71.8	170	52.7	297	98.2	41.4	32.59	99.8	96.3
Py2									
QPY-1	-	-	-	-	0.55	6.53	50.2	-	-
QPY-2	-	-	0.59	0.11	0.45	7.30	9.50	1.70	-
QPY-3	-	-	-	-	-	2.59	-	1.63	-
QPY-4	0.27	1.10	49.7	53.0	1.26	100	8.30	-	1.44
QPY-5	0.02	0.04	0.60	0.17	0.62	2530	23.0	55.5	-
QPY-6	-	-	0.83	0.09	0.54	1830	28.4	19.4	-
QPY-7	4.00	360	2700	82,000	7.30	5.63	7.50	-	2.50
QPY-8	1.18	21.5	19.6	69.0	0.80	367	99.4	6.60	-
QPY-9	0.08	-	0.72	0.251	0.61	328	192	2.46	11.2
QPY-10	-	-	0.67	0.22	0.42	388	159	-	2.51
QPY-11	-	0.02	0.42	0.26	-	245	40.4	-	14.8
QPY-12	-	-	-	0.07	0.43	2330	72.9	13.3	1.06
QPY-13	-	-	0.30	0.17	0.38	295	236	3.15	8.60
QPY-14	-	-	0.28	0.05	-	99.4	71.1	2.27	10.3
QPY-15	-	0.01	0.83	-	-	3.13	0.54	-	-
QPY-16	5.00	103	460	340	270	2.66	24.9	-	3.60
QPY-17	1.06	2.41	5.40	2.80	-	587	73.8	19.9	7.70
QPY-18	0.05	1.14	0.48	760	0.69	44.0	59	-	34.6
QPY-19	2.71	167	71.0	18,700	405	2.22	62.1	-	20.4
QPY-20	0.16	101	2090	500	217	1240	70	18.4	55.3
QPY-21	-	-	0.45	0.06	-	47.8	2.32	1.80	42.2
Average	1.45	68.8	300	5690	60.4	498	64.5	12.2	15.4
RSD	125	163.5	259	343	212	158	99.9	128	110

Note: RSD—relative standard deviation; “-” means below detection limit.

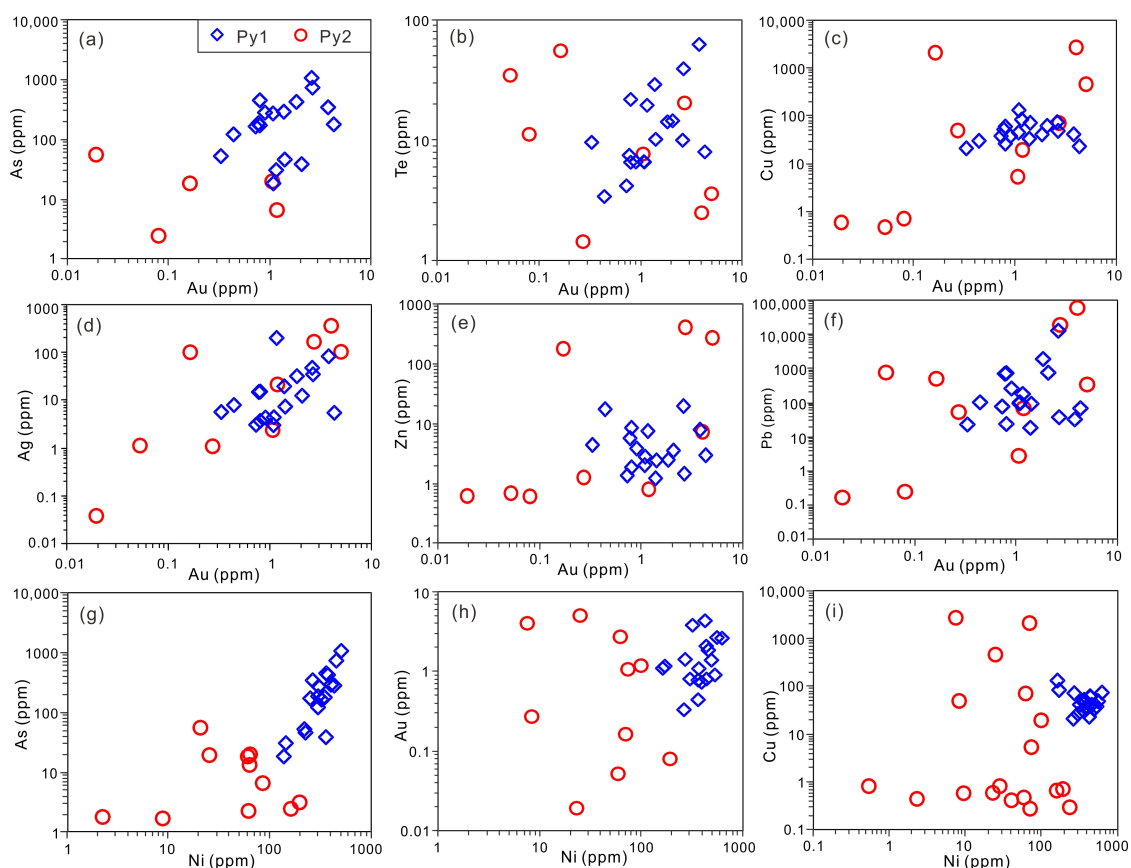


Figure 4. Scatterplots of (a) As vs. Au, (b) Te vs. Au, (c) Cu vs. Au, (d) Ag vs. Au, (e) Zn vs. Au, (f) Pb vs. Au, (g) As vs. Ni, (h) Au vs. Ni, and (i) Cu vs. Ni in the two types of pyrite (Py1 and Py2) from the Huanxiangwa deposit.

The trace-element results reveal that the concentrations of most elements analyzed were relatively constant in Py1 but show variations of up to several orders of magnitude in Py2. The relative standard deviation (RSD) indicates the extent of variability in relation to the mean of the population. This measure is often expressed as a percentage and is defined as the ratio of the standard deviation to the mean. The RSD values of Au, Cu, Zn, Co, Ni, As, and Te were lower than 100% in Py1, whereas the values (except for Ni) in Py2 exceeded 100%. Py1 contained significant amounts of Pb, Co, Ni, and As with trace Zn, Ag, Cu, Au, and Te. Py2 contained significant amounts of Cu, Pb, and Co with trace Zn, Ag, As, Au, and Te. The pyrite generally contained low Au concentrations, ranging from 0.33 to 4.30 ppm (mean 1.56 ppm) in Py1 and from <0.02 to 5.00 ppm (mean 1.45 ppm) in Py2. The pyrite contained abundant amounts of Co and Ni, with Co contents of 181–830 ppm in Py1 and 2.22–2530 ppm in Py2 and Ni contents of 163–627 ppm in Py1 and 0.54–236 ppm in Py2.

Ni and As occurred at higher concentrations in Py1 than in Py2, whereas Cu, Pb, Zn, and Ag occurred at higher concentrations in Py2 than in Py1 (Table 1). Au, Co, and Te were more uniformly distributed among samples of the two pyrite types. The plots of Au versus other elements (Figure 4) and the associated correlation coefficients (Tables 2 and 3) show positive linear correlations of Au with As, Te, Ag, and Ni in Py1 and of Au with Cu, Pb, Zn, and Ag in Py2 as well as a negative correlation between Au and Co in Py2.

Table 2. Correlation coefficients between trace elements in Py1 from the Huanxiangwa gold deposits.

Element	Au	Ag	Cu	Pb	Zn	Co	Ni	As
Ag	0.44							
Cu	0.19	0.21						
Pb	0.18	0.15	0.45					
Zn	−0.08	0.29	0.18	0.52				
Co	0.18	0.20	0.81	0.57	0.43			
Ni	0.31	−0.07	−0.33	0.35	−0.02	−0.08		
As	0.33	0.14	−0.29	0.27	0.08	−0.06	0.82	
Te	0.55	0.73	−0.02	−0.29	−0.21	−0.18	0.03	0.21

Table 3. Correlation coefficients between trace elements in Py2 from the Huanxiangwa gold deposits.

Element	Au	Ag	Cu	Pb	Zn	Co	Ni	As
Ag	0.81							
Cu	0.68	0.88						
Pb	0.63	0.87	0.83					
Zn	0.60	0.73	0.79	0.71				
Co	−0.71	−0.29	−0.28	−0.55	−0.44			
Ni	−0.22	0.41	−0.06	−0.11	−0.13	0.48		
As	−0.29	−0.77	0.41	0.33	0.29	0.83	0.14	
Te	−0.48	−0.06	−0.20	0.07	0.39	−0.05	0.01	−0.23

7. Discussion

7.1. Gold Distribution in Py1

Although visible gold is recognized in Py1 from the Huanxiangwa deposit, the amounts do not tend to correspond to the gold assay data for bulk rock samples [38,39], meaning that some gold in Py1 is likely to be present as invisible gold. LA-ICP-MS output data for each laser spot analysis can be inspected to ascertain whether a particular trace element occurs in homogeneously distributed invisible form or as nano- to submicron-sized inclusions in pyrite [19,42]. To examine the occurrence of invisible gold in the Huanxiangwa deposit pyrite, we disregarded the visible gold grains, and therefore the measured Au concentrations are rather low. Representative LA-ICP-MS time-resolved depth profiles for Py1 are presented in Figure 5.

A total of 18 Py1 spots contained measurable quantities of gold. The dataset shows that gold concentrations are relatively uniform among the samples (Table 1). Gold distribution patterns for most samples are relatively smooth (Figure 5a–c) with no obvious spikes, meaning that gold occurs primarily as solid solution in the pyrite lattice or as homogeneously distributed nanoparticles in pyrite [19,20]. A small number of Py1 grains show spiky depth-concentration profiles for Au, Ag, and Te (Figure 5d), suggesting the presence of nano- to submicron-sized inclusions of native gold, electrum, and/or Au-Ag-Te minerals in Py1 grains.

Arsenic likely enters the structure of pyrite by the substitution of As³⁺ for S^{2−} to form Fe(As,S)₂, a typical mechanism under reducing conditions, or by a substitution involving the coupling of As with Au (e.g., Au⁺ + As³⁺ ↔ 2Fe²⁺) [43–47]. The structure of pyrite becomes distorted when As is incorporated, favoring the entry of relatively large Au⁺ ions into the structure [17,18,21]. Thus, the adsorption of gold complexes onto As-rich pyrite surfaces is considered a key process in the deposition of gold from fluid [17,45,47]. Furthermore, the incorporation of Te might also distort the pyrite lattice, allowing Au to enter instead of, or together with, As [19,23,48]. The abundance of As in most Py1 samples (Table 1) suggests that Py1 is As bearing. Gold shows a positive correlation with As and Te in Py1 (Figure 4a,b; Table 2), suggesting that the incorporation of Au into Py1 in the Huanxiangwa deposit was largely controlled by the presence and behavior of As and Te.

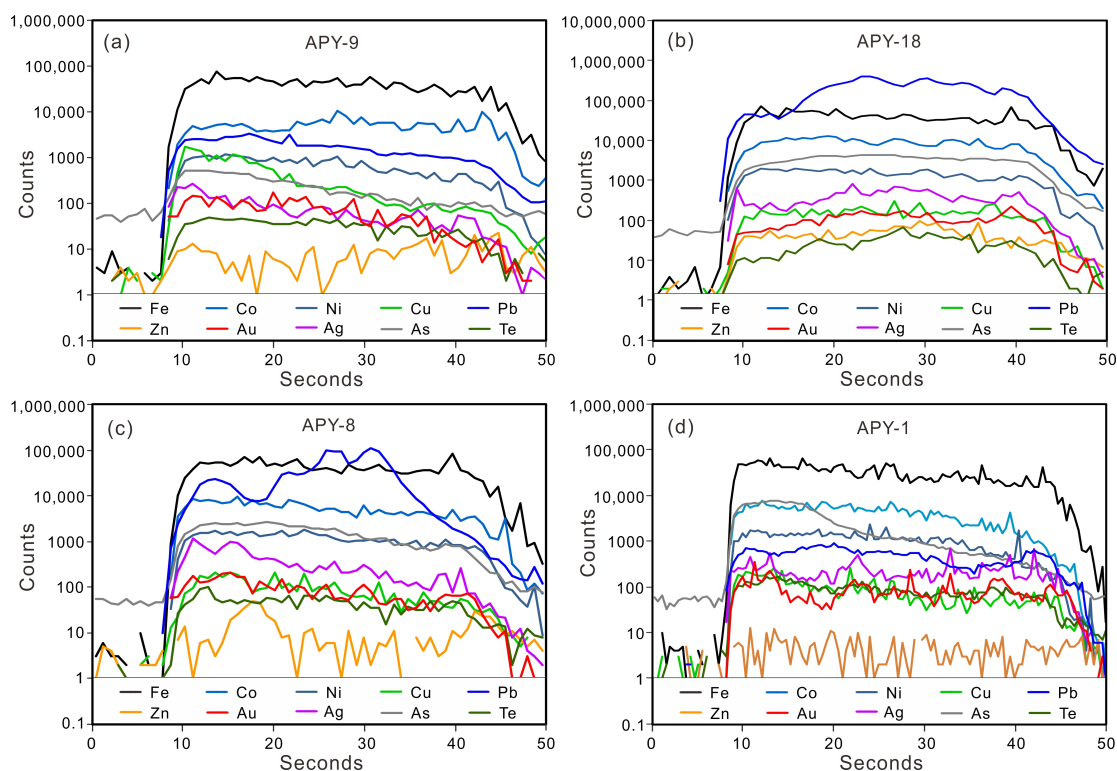


Figure 5. LA-ICP-MS time-resolved depth profiles for Py1 from selected samples showing the occurrences of Au and other elements. The smooth time-resolved depth profiles for Au and Ag (a–c) reflect solid-solution gold and electrum in Py1. The spiky time-resolved depth profiles for Au, Ag, and Te (d) suggest that some Py1 grains contain small amounts of native Au, electrum, and/or Au-Ag-Te minerals as nano- to submicron-sized inclusions.

7.2. Gold Distribution in Py2

The results show that both visible and invisible gold occurs in Py2 from the Huanxiangwa deposit. Similar to Py1, visible gold in Py2 occurs as native gold and electrum in fractures or as inclusions.

The absolute values of As in Py2 are low, ranging from levels below the detection limit to 55.5 ppm. Measured Te concentrations in Py2 are also low, ranging from 1.06 to 55.3 ppm, with a mean of 15.4 ppm. Furthermore, there is no discernable correlation of Au with As or Te (Figure 4a,b; Table 3). These observations indicate that As and Te were not important scavengers of gold during the development of the auriferous quartz-vein-type ores in the Huanxiangwa deposit. The occurrence of invisible gold in Py2 is therefore of particular significance because the pyrite contains very low levels of As and Te. These results contradict the conventional view that the presence of these elements assists the incorporation of gold into pyrite [17–19,21,44].

Most of the LA-ICP-MS time-resolved depth profiles for Au in Py2 are wavy, displaying several spikes (Figure 6a,b), indicating the occurrence of Au in Py2 as nano- to submicron-sized inclusions. Notably, the absolute values of Cu, Pb, Zn, and Ag show that these elements are abundant in Py2 and vary markedly from levels below the detection limit to several hundreds or thousands of ppm (Table 1). All of these elements show positive correlations with Au (Figure 4; Table 3). Moreover, the spikes of Cu, Pb, Zn, and Ag observed in the time-resolved depth profiles (Figure 6c,d) are similar to those of Au in most samples, suggesting that gold occurs in the form of complex Au-Cu-Pb-Zn-Ag nano- to submicron-sized inclusions in Py2. Considering that Py2 is poor in As and Te and shows strong associations of Au with Cu, Pb, Zn, and Ag, the occurrence of invisible gold in Py2 implies that some or all of the elements (Cu, Pb, Zn, and Ag) might have assisted the incorporation of Au into pyrite, although the particular mechanism involved is still unknown. This proposed process has also been reported in gold deposits elsewhere [19,49].

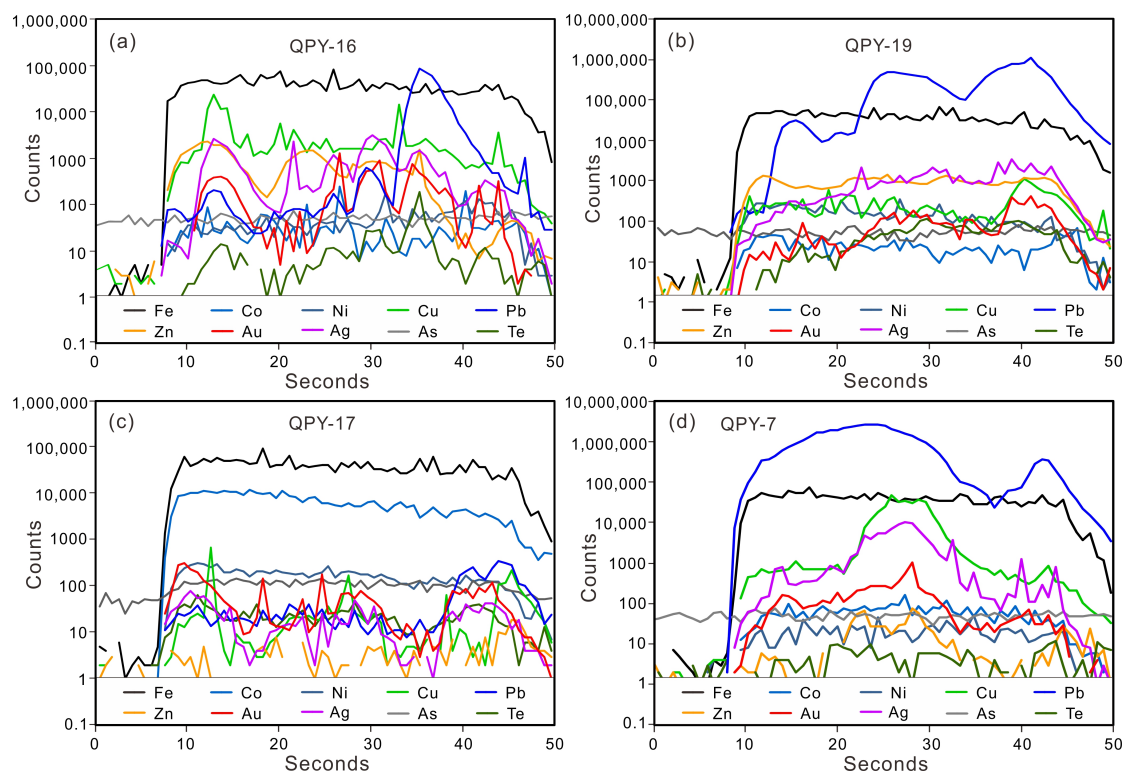


Figure 6. LA-ICP-MS time-resolved depth profiles for Au in Py2 display several spikes (a,b), indicating the occurrence of Au in Py2 as nano- to submicron-sized inclusions. Spikes of Cu, Pb, Zn, and Ag in the profiles are similar to those of Au in most samples (c,d), suggesting that gold occurs as complex Au-Cu-Pb-Zn-Ag nano- to submicron-sized inclusions in Py2.

7.3. Implication for Ore Genesis

Although the gold deposits in the Xiong’ershan district have been well studied, their genesis remains debated. The main issue is the source of the ore-forming fluids. On the basis of the structural setting and fluid geochemistry of the Xiong’ershan district, most investigators have classified the deposits as orogenic gold deposits and have suggested that the gold-mineralizing fluids were derived mainly from metamorphic dehydration reactions [3,5,9]. Considering the temporal and spatial relationships between the gold deposits and the magmatic intrusions, some investigators have proposed that gold mineralization in the Xiong’ershan district resulted from Early Cretaceous magmatic-hydrothermal processes [6,7,10,11]. In contrast, other studies have suggested that the gold deposits are greenstone type deposits [8], with basement metamorphic rocks being the source for the gold [2]. However, there is a time gap of approximately 2 Gyr between the metamorphism and the gold mineralization [50], and therefore we disregard this hypothesized metamorphism-related genesis.

The two types of pyrite in the Huanxiangwa gold deposit exhibit contrasting sizes, textures, and crystal forms and also differ in terms of their host rocks. These two types of pyrite also differ with respect to their trace-element concentrations and gold occurrences. These contrasting characteristics indicate that the two types of pyrite precipitated from different hydrothermal fluid systems.

The Co and Ni contents of pyrite can reflect its origin and reveal the geological setting of its formation [15,19,51]. The majority (apart from two samples) of the Co/Ni ratios of Py1 range from 0.60 to 1.67 (Table 1), with a mean of 1.04, similar to metamorphic pyrite [52,53]. Fluid inclusions from type 1 ores at the Huanxiangwa deposit have high CO₂ contents (7.45 mol %–15.6 mol %) and low salinities (5 wt %–11 wt %) [39], which are typical of metamorphic-hydrothermal fluid systems [5,54,55]. Therefore, we infer that Py1 was precipitated from this type of fluid system. Conversely, the Co/Ni ratios of Py2 in auriferous quartz veins range from 0.04 to 110, with a mean of 14.5 (Table 1), typical of magmatic-hydrothermal pyrite and consistent with ratios measured in Early Cretaceous magmatic

rocks [37]. Type 2 ores at Huanxiangwa contain halite-bearing, liquid-rich, and CO₂-bearing fluid inclusions [39], which is a common fluid inclusion assemblage in typical magmatic-hydrothermal deposits. Sulfur isotopes of Py2 (mostly from −3.4‰ to +0.6‰) [39] and the presence of fluorite further confirm a magmatic origin for Py2 in the Huanxiangwa deposit.

Nickel can be readily incorporated into the crystal lattice of pyrite but is not easily released during the recrystallization of hydrothermal pyrite [56–58]. Therefore, the patterns of Ni distribution in pyrite should yield information about the pyrite-precipitating fluid [48]. Ultramafic (and to a lesser extent mafic) rocks exhibit strong enrichment in Ni, whereas felsic rocks typically have low Ni contents. Therefore, pyrite from granite-related gold deposits should contain only small amounts of Ni, and high Ni contents should indicate a high proportion of mafic-ultramafic rocks compared with felsic rocks in the fluid source domain [48]. In the Huanxiangwa deposit, the Ni concentrations of Py1 reach up to 627 ppm (mean 387 ppm). The high Ni contents of Py1 at Huanxiangwa might reflect local leaching of the mafic basement rocks of the Xiong'er district. In contrast, the absolute values of Ni in Py2 are relatively low (mean 64.5 ppm), suggesting that Py2 was precipitated from granite-related hydrothermal fluids.

The disseminated ores (type 1 ores) are cut by auriferous quartz veins (type 2 ore) (Figure 3c) in the Huanxiangwa deposit, indicating that type 1 ores formed earlier than type 2 ores. The available geochronological data suggest that the Mesozoic gold mineralization in the Xiong'er district occurred during two main periods: Triassic (242–202 Ma, mainly 222–202 Ma) [5,59,60] and Early Cretaceous (135–110 Ma) [6,10,11,59]. The Triassic ages are chiefly from the minerals within the disseminated ores (e.g., Shanggong and Dianfang deposits), whereas the Early Cretaceous ages are mainly from minerals within alteration zones around quartz veins.

Based on our field and petrographic observations, our LA-ICP-MS analysis results, and previous geochronological data, we conclude that the Huanxiangwa gold deposit was formed during two episodes of hydrothermal mineralization events associated with two distinct source reservoirs. The first episode took place during the Triassic, shortly after the collision of the NCC with the Yangtze Craton [12,48]. The ore-forming fluids originated from the metamorphic dehydration of basement ultramafic to mafic rocks. This metamorphism-derived fluid reacted with the Fe²⁺-rich andesite in the Xiong'er Group, which led to the precipitation of Py1 and gold in the altered andesite to form disseminated ores (type 1 ores). The second episode occurred during the Early Cretaceous, when lithospheric thinning triggered the intrusion and emplacement of various granitic bodies and porphyry stocks in the Xiong'er district [6,7,31–34]. Py2 was formed during the related ensuing magmatic-hydrothermal activity and was precipitated as coarse euhedral grains dispersed in auriferous quartz veins, as indicated by low Ni, As, and Te contents in Py2 and the presence of fluorite.

8. Conclusions

Pyrite is the dominant Au-bearing mineral in the Huanxiangwa gold deposit and can be classified into two types: (1) medium- to fine-grained subhedral-anhedral pyrite (Py1) disseminated in altered rocks and (2) coarse-grained, subhedral-euhedral pyrite (Py2) hosted in auriferous quartz veins.

Petrographic observations indicate that both visible and invisible gold are present in the pyrite. Visible gold occurs as native gold and electrum and commonly forms anhedral grains within pyrite as well as along boundaries within or between mineral microfractures. LA-ICP-MS depth profiles indicate that invisible gold occurs primarily as solid solution or as homogeneously distributed nanoparticles of native gold, electrum, or Au-Ag-Te minerals in Py1 but is present mainly as nano- to submicron-sized inclusions of complex Au-Cu-Pb-Zn-Ag domains in Py2.

The data presented here, together with previous geochronological information, suggest that the Huanxiangwa gold deposit was a result of two episodes of hydrothermal mineralization associated with two distinct source reservoirs. The first episode of mineralization occurred during the Triassic and resulted from the collision of the NCC with the Yangtze Craton. The ore-forming fluids were derived from the metamorphic dehydration of ultramafic-mafic basement rocks. The second episode

of mineralization took place during Early Cretaceous and was related to the development of felsic magmatic-hydrothermal fluids.

Author Contributions: F.G. collected the samples and studied the sulfides using LA-ICPMS. All authors (F.G., Y.D., Z.P., Y.D., F.X., and J.X.) discussed the results and evaluated the data. F.G. wrote and organized the paper. F.X. and J.X. provided geological information and granted access to the mine.

Funding: This research was funded by the National Natural Science Foundation of China, grant number 41403032, and the China Geological Survey, grant number 12120113083000.

Acknowledgments: Senior Engineers Weizhi Sun and Jianhui Xiao and Master Students Xiaowei Zhang, Shaolei Kou, and Hongxiang Jia provided valuable assistance in the field.

Conflicts of Interest: The authors declare no conflict of interest.

References

1. Groves, D.I.; Goldfarb, R.J.; Santosh, M. The conjunction of factors that lead to formation of giant gold provinces and deposits in non-arc settings. *Geosci. Front.* **2016**, *7*, 303–314. [[CrossRef](#)]
2. Li, S.R.; Santosh, M. Geodynamics of heterogeneous gold mineralization in the North China Craton and its relationship to lithospheric destruction. *Gondwana Res.* **2017**, *50*, 267–292. [[CrossRef](#)]
3. Mao, J.W.; Goldfarb, R.J.; Zhang, Z.W.; Xu, W.Y.; Qiu, Y.M.; Deng, J. Gold deposits in the Xiaolinling–Xiong’ershan region, Qinling mountains, Central China. *Miner. Depos.* **2002**, *37*, 306–325. [[CrossRef](#)]
4. Deng, J.; Gong, Q.; Wang, C.; Carranza, E.J.M.; Santosh, M. Sequence of Late Jurassic–Early Cretaceous magmatic-hydrothermal events in the Xiong’ershan region, Central China: An overview with new zircon U–Pb geochronology data on quartz porphyries. *J. Asian Earth Sci.* **2014**, *79*, 161–172. [[CrossRef](#)]
5. Chen, Y.J.; Pirajno, F.; Qi, J.P. The Shangong gold deposit, Eastern Qinling Orogen, China: Isotope geochemistry and implications for ore genesis. *J. Asian Earth Sci.* **2008**, *33*, 252–266. [[CrossRef](#)]
6. Tang, K.F.; Li, J.W.; Selby, D.; Zhou, M.F.; Bi, S.J.; Deng, X.D. Geology, mineralization, and geochronology of the Qianhe gold deposit, Xiong’ershan area, southern North China Craton. *Miner. Depos.* **2013**, *48*, 729–747. [[CrossRef](#)]
7. Tian, Y.F.; Sun, J.; Ye, H.S.; Mao, J.W.; Wang, X.X.; Bi, M.F.; Xia, X.P. Genesis of the Dianfang breccia-hosted gold deposit, western Henan Province, China: Constraints from geology, geochronology and geochemistry. *Ore Geol. Rev.* **2017**, *91*, 963–980. [[CrossRef](#)]
8. Li, S.M.; Qu, L.Q.; Su, Z.B.; Huang, J.J.; Wang, X.S.; Yue, Z.S. *The Geology and Metallogenic Prediction of the Gold Deposit in Xiaolinling*; Geological Publishing House: Beijing, China, 1996; pp. 67–178. (In Chinese)
9. Goldfarb, R.J.; Phillips, G.N.; Nokleberg, W.J. Tectonic setting of synorogenic gold deposits of the Pacific Rim. *Ore Geol. Rev.* **1998**, *13*, 185–218. [[CrossRef](#)]
10. Yao, J.M.; Zhao, T.P.; Li, J.; Sun, Y.L.; Yuan, Z.L.; Chen, W.; Han, J. Molybdenite Re–Os age and zircon U–Pb age and Hf isotope geochemistry of the Qiyugou gold system, Henan province. *Acta Petrol. Sin.* **2009**, *25*, 374–384.
11. Zhai, L.; Liu, Y.G.; Jiao, Y.H. Geological features and ore-forming age of Miaoling gold deposit in Henan. *Jinlin Geol.* **2011**, *30*, 34–40. (In Chinese with English abstract).
12. Tang, L.; Zhang, S.T.; Yang, F.; Santosh, M.; Li, J.J.; Kim, S.W.; Hu, X.K.; Zhao, Y.; Cao, H.W. Triassic alkaline magmatism and mineralization in the Xiong’ershan area, East Qinling, China. *Geol. J.* **2018**. [[CrossRef](#)]
13. Zhang, G.W.; Meng, Q.G.; Yu, Z.P.; Sun, Y.; Zhou, D.W.; Guo, A.L. Orogenesis and dynamics of the Qinling orogen. *Sci. China Ser. D* **1996**, *39*, 225–234.
14. Craig, J.R.; Vokes, F.M.; Solberg, T.N. Pyrite: Physical and chemical textures. *Miner. Depos.* **1998**, *57*, 3–18. [[CrossRef](#)]
15. Agangi, A.; Hofmann, A.; Wohlgemuth-Ueberwasser, C.C. Pyrite Zoning as a Record of Mineralization in the Ventersdorp Contact Reef, Witwatersrand Basin, South Africa. *Econ. Geol.* **2013**, *108*, 1243–1272. [[CrossRef](#)]
16. Keith, M.; Smith, D.J.; Jenkin, G.R.T.; Holwell, D.A.; Dye, M.D. A review of Te and Se systematics in hydrothermal pyrite from precious metal deposits: Insights into ore-forming processes. *Ore Geol. Rev.* **2018**, *96*, 269–282. [[CrossRef](#)]
17. Deditius, A.P.; Reich, M. Constraints on the solid solubility of Hg, Tl, and Cd in arsenian pyrite. *Am. Miner.* **2016**, *101*, 1451–1459. [[CrossRef](#)]

18. Simon, G.; Huang, H.; Penner-Hahn, J.E.; Kesler, S.E.; Kao, L.S. Oxidation state of gold and arsenic in gold-bearing arsenian pyrite. *Am. Miner.* **1999**, *84*, 1071–1079. [[CrossRef](#)]
19. Cook, N.J.; Ciobanu, C.L.; Mao, J.W. Textural control on gold distribution in As-free pyrite from the Dongping, Huangtuliang and Hougou gold deposits, North China craton (Hebei Province, China). *Chem. Geol.* **2009**, *264*, 101–121. [[CrossRef](#)]
20. Sung, Y.H.; Brugger, J.; Ciobanu, L.; Pring, A.; Skinner, W.; Nugus, M. Invisible gold in arsenian pyrite and arsenopyrite from a multistage Archaean gold deposit: Sunrise Dam, Eastern Goldfields Province, Western Australia. *Miner. Depos.* **2009**, *44*, 765–791. [[CrossRef](#)]
21. Morishita, Y.; Shimada, N.; Shimada, K. Invisible gold in arsenian pyrite from the high-grade Hishikari gold deposit, Japan: Significance of variation and distribution of Au/As ratios in pyrite. *Ore Geol. Rev.* **2018**, *95*, 79–93. [[CrossRef](#)]
22. Deditius, A.P.; Utsunomiya, S.; Renock, D.; Ewing, R.C.; Ramana, C.V.; Becker, U.; Kesler, S.E. A proposed new type of arsenian pyrite: Composition, nanostructure and geological significance. *Geochim. Cosmochim. Acta* **2008**, *72*, 2919–2933. [[CrossRef](#)]
23. Bi, S.J.; Li, J.W.; Zhou, M.F.; Li, Z.K. Gold distribution in As-deficient pyrite and telluride mineralogy of the Yangzhaiyu gold deposit, Xiaoqinling district, southern North China craton. *Miner. Depos.* **2011**, *46*, 925–941. [[CrossRef](#)]
24. Deng, X.H.; Chen, Y.J.; Santosh, M.; Yao, J.M. Genesis of the 1.76 Ga Zhaiwa Mo–Cu and its link with the Xiong'er volcanics in the North China Craton: Implications for accretionary growth along the margin of the Columbia supercontinent. *Precambrian Res.* **2013**, *227*, 337–348. [[CrossRef](#)]
25. Santosh, M. Assembling North China Craton within the Columbia supercontinent: The role of double-sided subduction. *Precambrian Res.* **2010**, *178*, 149–167. [[CrossRef](#)]
26. Huang, X.L.; Wilde, S.A.; Yang, Q.J.; Zhong, J.W. Geochronology and petrogenesis of gray gneisses from the Taihua Complex at Xiong'er in the southern segment of the trans-north china orogen: Implications for tectonic transformation in the early paleoproterozoic. *Lithos* **2012**, *134–135*, 236–252. [[CrossRef](#)]
27. Kröner, A.; Compston, W.; Zhang, G.W.; Guo, A.L.; Todt, W. Age and tectonic setting of Late Archean greenstone-gneiss terrain in Henan Province, China, as revealed by single-grain zircon dating. *Geology* **1988**, *16*, 211–215. [[CrossRef](#)]
28. Xu, X.S.; Griffin, W.L.; Ma, X.; O'Reilly, S.Y.; He, Z.Y.; Zhang, C.L. The Taihua group on the southern margin of the North China craton: Further insights from U–Pb ages and Hf isotope compositions of zircons. *Miner. Petrol.* **2009**, *97*, 43–59. [[CrossRef](#)]
29. Zhao, T.P.; Zhai, M.G.; Xia, B.; Li, H.M.; Zhang, Y.X.; Wan, Y.S. Zircon U–Pb SHRIMP dating for the volcanic rocks of the Xiong'er Group: Constraints on the initial formation age of the cover of the North China Craton. *Chin. Sci. Bull.* **2004**, *22*, 2342–2349, (In Chinese with English abstract). [[CrossRef](#)]
30. He, Y.H.; Zhao, G.C.; Sun, M.; Xia, X.P. SHRIMP and LA-ICP-MS zircon geochronology of the Xiong'er volcanic rocks: Implications for the Paleo-Mesoproterozoic evolution of the southern margin of the North China Craton. *Precambrian Res.* **2009**, *168*, 213–222. [[CrossRef](#)]
31. Mao, J.W.; Xie, G.Q.; Pirajno, F.; Ye, H.S.; Wang, Y.B.; Li, Y.F.; Xiang, J.F.; Zhao, H.J. Late Jurassic–Early Cretaceous granitoid magmatism in Eastern Qinling, central-eastern China: SHRIMP zircon U–Pb ages and tectonic implications. *Aust. J. Earth Sci.* **2010**, *57*, 51–78. [[CrossRef](#)]
32. Gao, X.Y.; Zhao, T.P.; Yuan, Z.L.; Zhou, Y.Y.; Gao, J.F. Geochemistry and petrogenesis of the Heyu batholith in the southern margin of the North China block. *Acta Petrol. Sin.* **2010**, *26*, 3485–3506.
33. Meng, F.; Ye, H.S.; Gao, Y.L. SHRIMP zircon U–Pb age and geological features of granites in the Xiong'ershan area, western Henan Province. *Miner. Depos.* **2012**, *31*, 591–592. (In Chinese)
34. Nie, Z.R.; Wang, X.X.; Ke, C.H.; Yang, Y.; Lv, X.Q. Age, geochemistry and petrogenesis of Huashan granitoid pluton on the southern margin of the North China Block. *Geol. Bull. China* **2015**, *34*, 1502–1516, (In Chinese with English abstract).
35. Han, Y.G.; Zhang, S.H.; Pirajno, F.; Wang, Y.; Zhang, Y.H. New $^{40}\text{Ar}/^{39}\text{Ar}$ age constraints on the deformation along the Machaoying fault zone: Implications for Early Cambrian tectonism in the North China Craton. *Gondwana Res.* **2009**, *16*, 255–263. [[CrossRef](#)]
36. Yan, J.S.; Pang, Z.S.; Yue, Z.S.; Zhang, Z.H. *The Tectonic Characteristics of Machaoying Fault Zone and Studies of Gold Mineralization*; Yellow River Conservancy Press: Zhengzhou, China, 2005; pp. 16–50. (In Chinese)

37. Gao, F.P.; Du, Y.S.; Pang, Z.S.; Du, Y.L.; Zong, Z.J.; Xie, J.S.; Xin, F.P. Late Jurassic to Early Cretaceous magmatism in the Xiong'ershan gold district, central China: Implications for gold mineralization and geodynamics. (unpublished; manuscript in preparation).
38. Wang, C.M.; Carranza, E.J.M.; Zhang, S.T.; Zhang, J.; Liu, X.J.; Zhang, D.; Sun, X.; Duan, C.J. Characterization of primary geochemical haloes for gold exploration at the Huanxiangwa gold deposit, China. *J. Geochem. Explor.* **2013**, *124*, 40–58. [[CrossRef](#)]
39. Gao, Y.L. Geology, Geochemistry and Genesis of Huanxiangwa Gold Deposit in Dongqinling, Henan Province. Master's Thesis, China University of Geosciences, Beijing, China, 2010.
40. Paton, C.; Hellstrom, J.; Paul, B.; Woodhead, J.; Hergt, J. Iolite: Freeware for the visualization and processing of mass spectrometer data. *J. Anal. Atom. Spectrom.* **2011**, *26*, 2508–2518. [[CrossRef](#)]
41. Longerich, H.; Jackson, S.; Gunther, D. Laser ablation inductively coupled plasma mass spectrometric transient signal data acquisition and analyte concentration calculation. *J. Anal. Atom. Spectrom.* **1996**, *11*, 899–904. [[CrossRef](#)]
42. Maslennikov, V.V.; Maslennikova, S.P.; Large, R.R.; Danyushevsky, L.V. Study of trace element zonation in vent chimneys from the Silurian Yaman-Kasay volcanic-hosted massive sulfide deposit (southern Urals, Russia) using laser ablation–inductively coupled plasma mass spectrometry (LA-ICPMS). *Econ. Geol.* **2009**, *104*, 1111–1141. [[CrossRef](#)]
43. Pals, D.W.; Spry, P.G.; Chryssoulis, S. Invisible gold and tellurium in arsenic-rich pyrite from the Emperor gold deposit, Fiji: Implications for gold distribution and deposition. *Econ. Geol.* **2003**, *98*, 479–493. [[CrossRef](#)]
44. Reich, M.; Kesler, S.E.; Utsunomiya, S.; Palenik, C.S.; Chryssoulis, S.L.; Ewing, R.C. Solubility of gold in arsenian pyrite. *Geochim. Cosmochim. Acta* **2005**, *69*, 2781–2796. [[CrossRef](#)]
45. Deditius, A.P.; Reich, M.; Kesler, S.E.; Utsunomiya, S.; Chryssoulis, S.L.; Walshe, J.; Ewing, R.C. The coupled geochemistry of Au and As in pyrite from hydrothermal ore deposits. *Geochim. Cosmochim. Acta* **2014**, *140*, 644–670. [[CrossRef](#)]
46. Stromberg, J.M.; Barr, E.; Van Loon, L.L.; Gordon, R.A.; Banerjee, N.R. Fingerprinting multiple gold mineralization events at the Dome mine in Timmins, Ontario, Canada: Trace element and gold content of pyrite. *Ore Geol. Rev.* **2019**, *104*, 603–619. [[CrossRef](#)]
47. Augustin, J.; Gaboury, D. Multi-stage and multi-sourced fluid and gold in the formation of orogenic gold deposits in the world-class Mana district of Burkina Faso – Revealed by LA-ICP-MS analysis of pyrites and arsenopyrites. *Ore Geol. Rev.* **2019**, *104*, 495–521. [[CrossRef](#)]
48. Zhao, H.X.; Frimmel, H.E.; Jiang, S.Y.; Dai, B.Z. LA-ICP-MS trace element analysis of pyrite from the Xiaoqinling gold district, China: Implications for ore genesis. *Ore Geol. Rev.* **2011**, *43*, 142–153. [[CrossRef](#)]
49. Frost, B.R.; Mavrogenes, J.A.; Tomkins, A.G. Partial melting of sulfide ore during medium- and high-grade metamorphism. *Can. Mineral.* **2002**, *40*, 1–18. [[CrossRef](#)]
50. Goldfarb, R.; Santosh, M. The dilemma of the Jiaodong gold deposits: Are they unique? *Geosci. Front.* **2014**, *5*, 139–153. [[CrossRef](#)]
51. Bralía, A.; Sabatini, G.; Troja, F. A reevaluation of the Co/Ni ratio in pyrite as geochemical tool in ore genesis problems. *Miner. Depos.* **1979**, *14*, 353–374. [[CrossRef](#)]
52. Chen, Y.J.; Zhai, M.G.; Jiang, S.Y. Significant achievements and open issues in study of orogenesis and metallogenesis surrounding the North China continent. *Acta Petrol. Sin.* **2009**, *25*, 2695–2726.
53. Mao, S.D.; Yang, R.S.; Qin, Y.; Guo, J.H. Characteristics of gold bearing mineral and occurrence of gold in the Yangshan gold deposit field, Gansu Province. *Acta Petrol. Sin.* **2009**, *25*, 2776–2790.
54. Groves, D.I.; Goldfarb, R.J.; Gebre-Mariam, M.; Hagemann, S.G.; Robert, F. Orogenic gold deposits: A proposed classification in the context of their crustal distribution and relationship to other gold deposit types. *Ore Geol. Rev.* **1998**, *13*, 7–27. [[CrossRef](#)]
55. Goldfarb, R.J.; Groves, D.I.; Cardoll, S. Orogenic gold and geologic time: A global synthesis. *Ore Geol. Rev.* **2001**, *18*, 1–75. [[CrossRef](#)]
56. Koglin, N.; Frimmel, H.E.; Minter, W.E.L.; Brätz, H. Trace-element characteristics of different pyrite types in Mesoarchean to Palaeoproterozoic placer deposits. *Miner. Depos.* **2010**, *45*, 259–280. [[CrossRef](#)]
57. Morse, J.W.; Luther, G.W. Chemical influences on trace metal-sulphide interactions in anoxic sediments. *Geochim. Cosmochim. Acta* **1999**, *63*, 3373–3378. [[CrossRef](#)]
58. Tribouillard, N.; Algeo, T.J.; Lyons, T.; Riboulleau, A. Trace metals as paleoredox and paleoproductivity proxies: An update. *Chem. Geol.* **2006**, *232*, 12–32. [[CrossRef](#)]

59. Tang, K.F. Characteristics, Genesis, and Geodynamic Setting of Representative Gold Deposits in the Xiong'ershan District, Southern Margin of the North China Craton. Ph.D. Thesis, China University of Geosciences, Wuhan, China, 2014. (In Chinese with English abstract).
60. Lu, X.X.; Li, M.L.; Wang, W.; Yu, Z.P.; Shi, Y.Z. Indosinian movement and metallogenesis in Qinling orogenic belt. *Miner. Depos.* **2008**, *27*, 762–773, (In Chinese with English abstract).



© 2019 by the authors. Licensee MDPI, Basel, Switzerland. This article is an open access article distributed under the terms and conditions of the Creative Commons Attribution (CC BY) license (<http://creativecommons.org/licenses/by/4.0/>).